Chapter 4

Post Processing Study of AGN Radiative Feedback: Main Results

In the previous sections we have introduced the two radiative transfer models (D and AD Model, see sections 2.3 and 2.4), and we have learnt some important properties. First of all, if we want to treat the radiative transfer in presence of a scattering medium, we cannot use the *D model*, because this one does not take into account the isotropic scattering of particles. As we have seen in chapter 3, early-type galaxies can have a large amount of hot X-ray emitting gas with many free-electrons, that scatter radiation isotropically. If we want to maintain a radiation feedback treatment at a minimum level of complexity, restricted to non-scattering medium, we can use the *D model* as written in section 2.3. In this section we will show the post processing study of the application of the two models mentioned above, with and without dust physics (see section 3.3), with the output of 2D hydro simulation of Ciotti, Pellegrini, et al. (2017).

To conclude we will compare our AD Model with another approach which we can find in Novak et al. (2012).

4.1 Study Case

In the following we are going to analyse the radiative transfer of AGN outburst using the D Model (2.3) and the AD Model (2.4). We have solved the differential equation numerically in post processing, using the output data of density, temperature and accretion luminosity of our hydro simulation (for detail see Ciotti, Pellegrini, et al. (2017)). We have taken four hydrodumps that represent critical situations (Fig. 4.1): just before an outburst (left panel), during an outburst with dust (second panel from the right), at the end the outburst (third panel from the left) and after the outburst (right panel); times are, respectively, 5.40 Gyr, 5.41 Gyr, 5.42 Gyr and 5.43 Gyr. The accretion luminosity in the outburst time is $\sim 5 \cdot 10^{43}$ (5.41 Gyr) .

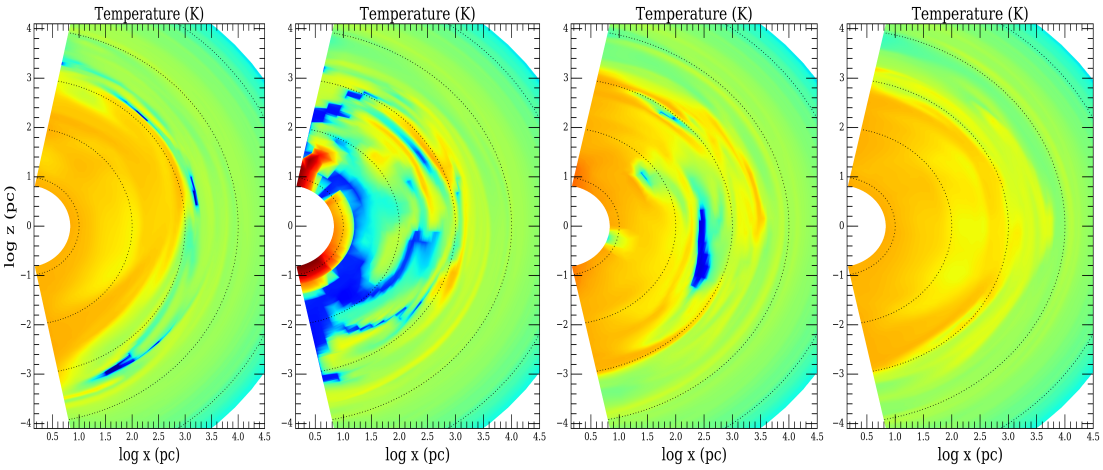

Figure 4.1: Temperature map in $Kelvin$. From the left to the right panel, respectively: 5.40 Gyr (before the AGN outburst),5.41 Gyr (during the AGN outburst), 5.42 Gyr and 5.43 Gyr (after the AGN outburst).

In Fig. 4.1 and Fig. 4.2 we can see respectively the temperature maps (in Kelvin degrees), the density maps (in particles per cm^3) and the radial velocity maps (in kms^{-1}). From the left to the right panel we can see that the gas dynamics is very complex: we have in some hydro dumps a nearly smooth situation, both in temperature and density; in the outburst situation, we can see the co-existence of inflow and outflow (we can distinguish them with the radial velocity maps). Moreover, this complexity is also present outside the region around the MBH, for example we can see in the first and third panel from the left that at $0.5 - 1$ kpc there can be some cold gas clouds.

So we have a spread in temperature of $\sim 10^5$ and in density we have a spread of $\sim 10^{10}$, therefore, the ISM changes optical regime very fast, both spatially and temporally, and as a consequence radiation couples with matter in very different ways.
We can see in Fig. 4.3 how the ISM opacity changes with hydrodynamics: in the first

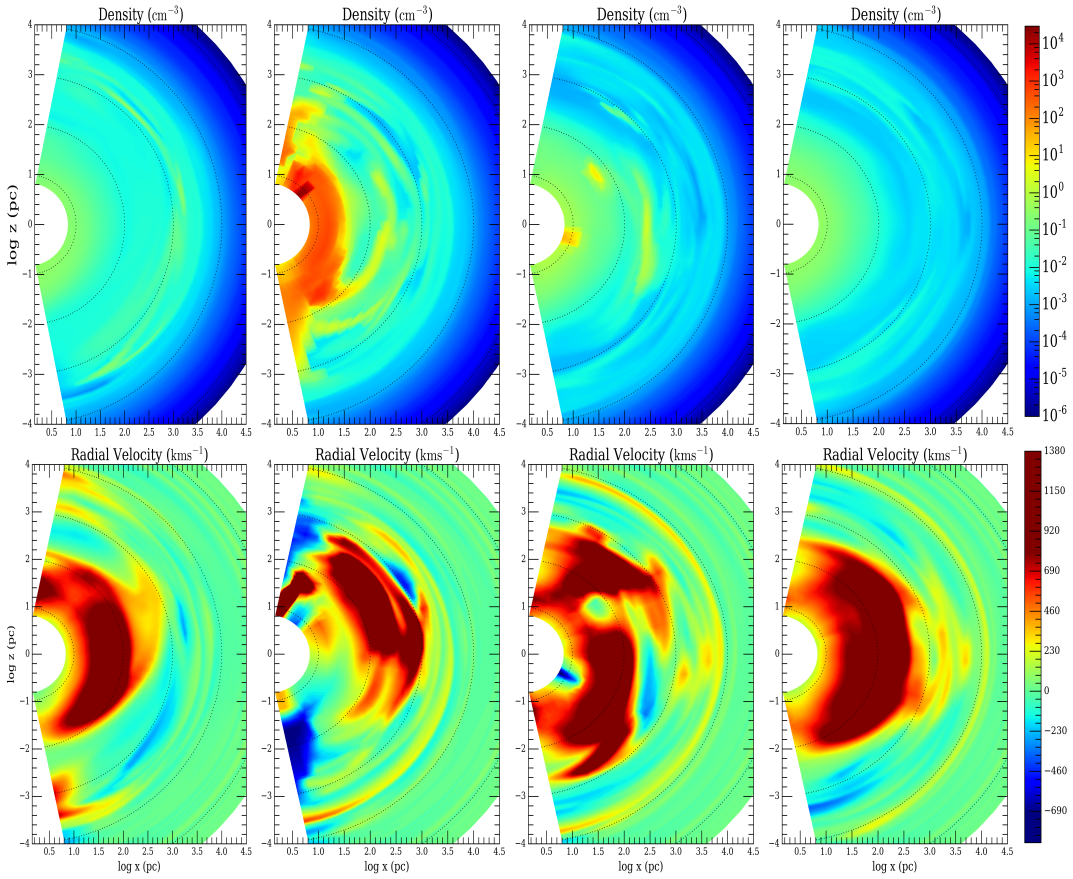

Figure 4.2: The top row is the density field (cm^{-3}), and the bottom row is the radial velocity field (kms^{-1}), both at the representative times of Fig. 4.1.

row we have computed the photoionization and Compton opacity, using the formula in 3.2 with the bolometric L_{BH} central boundary condition; in the bottom row, we show the total dust opacity (UV plus Optical band), using the 3.29. We can see clearly that dust and partially ionized clouds can coexist; depending on their density, we can have a optically thin or thick ISM. In the next section (4.2) we are going to apply the D Model to these characteristic times: first of all with only the presence of partially ionized clouds and with bolometric L_{BH}; after that, we will add dust opacity and we will divide the bolometric accretion luminosity in X, UV and Optical bands as we have seen in 3.3. Finally we will apply the AD Model (4.3) and then we will draw pro and contra of these models. We note that these outburst are very frequent during the lifetime of elliptical galaxies. We can see in Fig. 4.4 the run of L_{BH} *vs time*, when the luminosity values greater than $\sim 10^{42}$ show a quasar activity. As we can see from the accretion luminosity, there are lots of situations in which L_{BH} is over $\sim 10^{42}$ $ergs^{-1}$, and many others which are under this value; thus we expect many hydrodynamics changes with time, depending

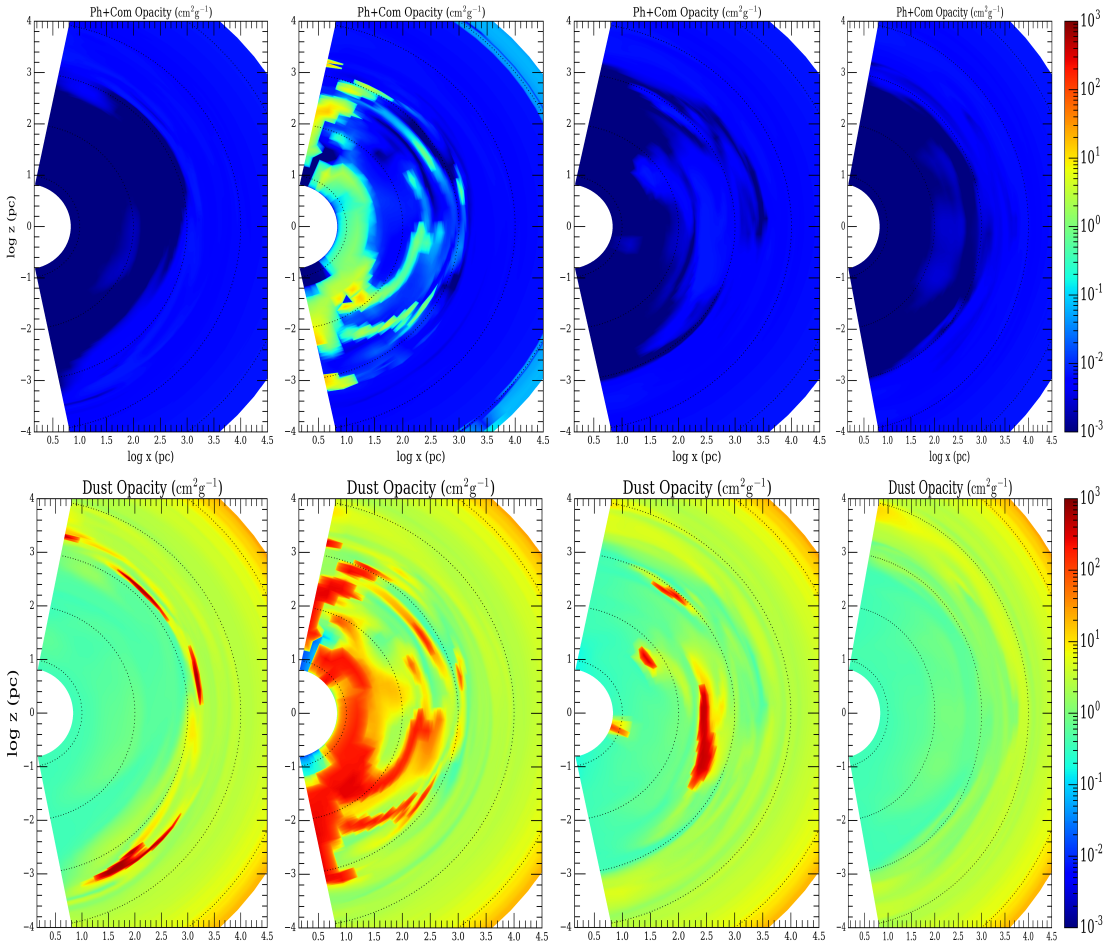

Figure 4.3: The top row is the *photoionization opacity* in cm^2g^{-1}; The bottom row is the *dust opacity* in cm^2g^{-1}. The times are the same as in 4.1.

on the quasar activity. If L_{BH} has a large value, it means that this large amount of energy can be transferred to the ISM (if the gas is optically thick) in some cases (for example, in the UV if there is dust), or it can escape away from the galaxy (if the gas is optically thin).

Moreover, we also have that when $10^{39} \leq L_{BH}\ erg/s \leq 10^{42}$ there is not a quasar activity, but however a remarkable amount of energy can be transferred to the ISM, and it can trigger some changes in hydrodynamics, that can impact on the accretion and as a consequence, quasar activity. In Fig. 4.5 we show the variation of L_{BH} (left panel) and L_X of the hot gas halo, from 5.38 Gyr to 5.45 Gyr. The variation in L_X of the hot halo shows us the quantity of gas present, and also the different phases of the flows in elliptical galaxies which can be *inflow*, *wind* and *outflow* (Ciotti, Ostriker, and Proga 2010).

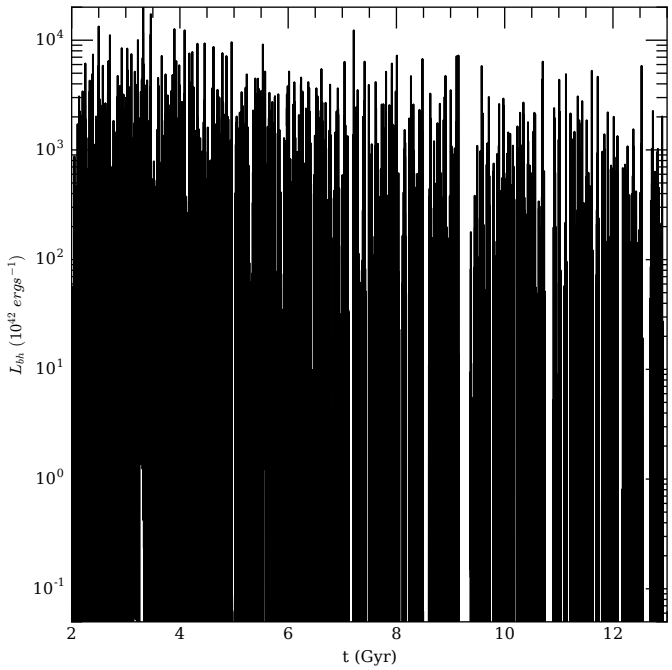

Figure 4.4: Accretion luminosity vs time from our simulations (for detail see Ciotti, Pellegrini, et al. (2017)).

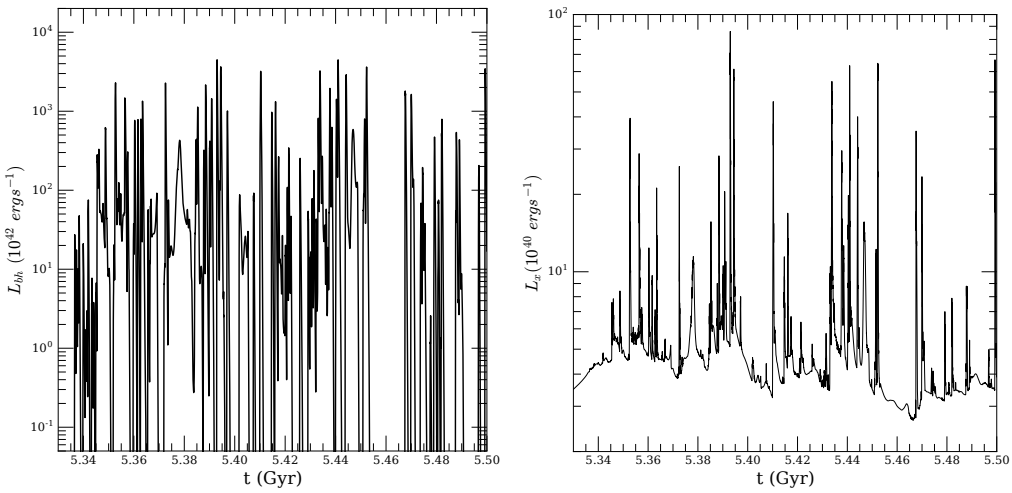

Figure 4.5: Left panel: accretion luminosity ($ergs^{-1}$) of Fig. 4.4 zoomed in the times which we have studied. Right panel: temperature (K) of the gas halo from ou simulations (for detail see Ciotti, Pellegrini, et al. (2017)).

4.2 D Model

4.2.1 Photoionization Physics

In the following we present the MBH luminosity maps and the gradient of radiation pressure on the ISM, applying the D Model modeling gas with only photoionization and line heating; (i.e. Sazonov, Ostriker, and Sunyaev 2004).
We have mapped the ratio of unabsorbed light and the total emitted light, in order to compare all maps with each other, to have an idea of the percentage of absorbed light, and then of the "absorbing power" of the medium.

We have also mapped the radiative pressure gradient: because of the large spread of these values ($\sim$ 40 orders of magnitude) is complex to draw conclusions on the impact on accretion evolution from post processing, but it can give us information on the different approaches of the two models. The complexity of drawing informations from the radiative pressure gradient comes from the fact that this is a radial force, which pushes (more or less) depending on the accretion luminosity and the ISM density and opacity. So in the next two sections we are trying to answers question such as:

a) Are there some differences with the addition of dust physics (3.3) and the division of bolometric MBH luminosity in bands (which increases computational time) with respect to the simple Sazonov (3.2) modeling of the ISM?

b) What are the main differences between the D Model and the more accurate AD Model in both ISM modeling?

We have four situations, as we have said before, in which the ISM is in some interesting

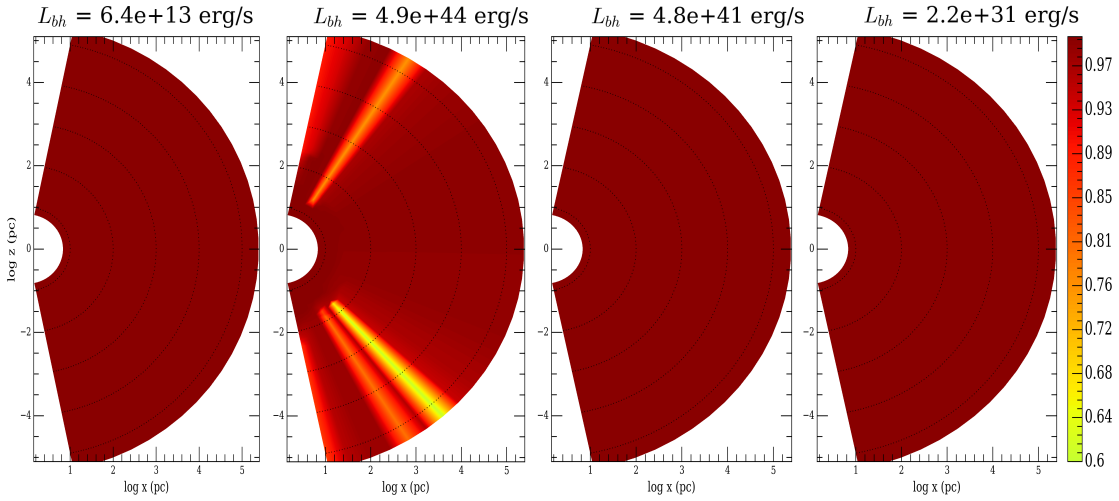

Figure 4.6: $L_{BH}^{eff}/L_{BH}^{bolo}$ with the D model in absence of dust. The times are the same as in 4.1.

thermodynamic state, and in which the L_{BH} varies a lot. If we take a look at Fig. 4.3 we can see that there is a greater opacity when L_{bh} is higher, and we have an optically

thin regime before and after the AGN outburst.
In the case of only photoionization and line heating of the ISM, we can see that in the cases of little opacity, the light absorbed is at most $\sim 5\%$, instead in the case of higher opacity, the absorbed light can reach $\sim 40\%$ (Fig. 4.6).

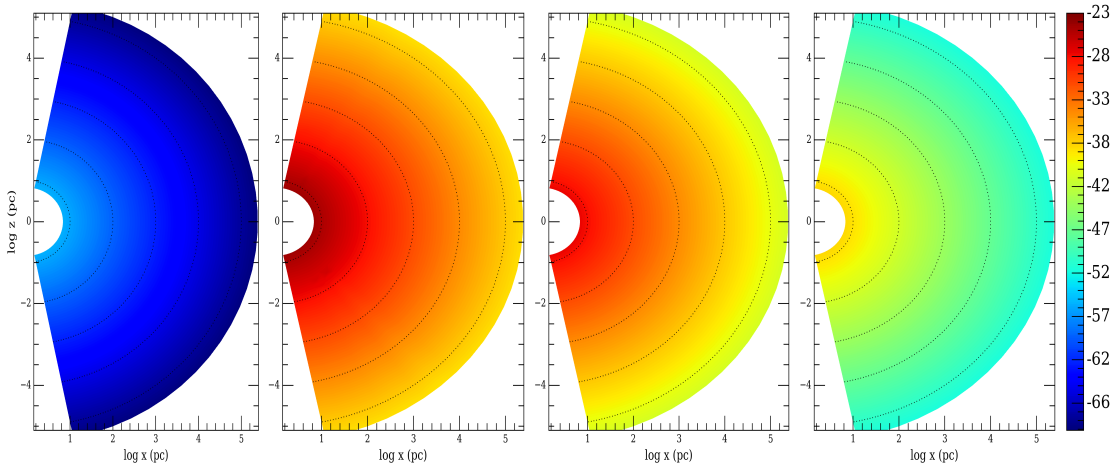

Figure 4.7: $log_{10}\nabla P_{RAD}$ $(cm\ g\ s^{-2})$ of $L^{eff}_{BH,bolo}$ with the D model in absence of dust. The times are the same as in 4.1.

For radial forces we can take a look at Fig. 4.7: here we have the global situation and we can see that when MBH is in the AGN phase (second and third panels from the left) the pressure gradient is higher than in situations in which the MBH is non active (first and fourth panels). The only situation in which ISM affect the variation of gradient pressure is the case more optically thick; because of the lineary dependence of the light (2.59), the cones in which light is absorbed can vary the pressure gradient of at most a value close to $\lesssim 1/2$ (because the maximum absorbed light in this case is $\lesssim 50\%$)

4.2.2 Photoionization and Dust Physics

Here we are going to add dust physics, in order to have a more realistic ISM. Despite elliptical galaxies have not dust in their quiescent and non-active phases, the existence of heavely absorbed quasars shows us that dust (and also cold gas) formation in these objects can be very common.

The processes at the base of dust formation in these objects is not yet completely clear. Probably, thermal instabilities can lead the gas to cool down and create the right environment for dust formation; another way to form dust can be through red giant and final stages of stars (as we have seen in section 3.3).

In Fig. 4.3 we can see the dust opacity, and where the gas density is high (Fig. 4.2) we can have a $\tau > 1$ and so, an optically thick regime. Generally, dust optical depth is higher than photoionization optical depth.

We briefly recall the dust opacity (in cgs system) and the amount of energy in each

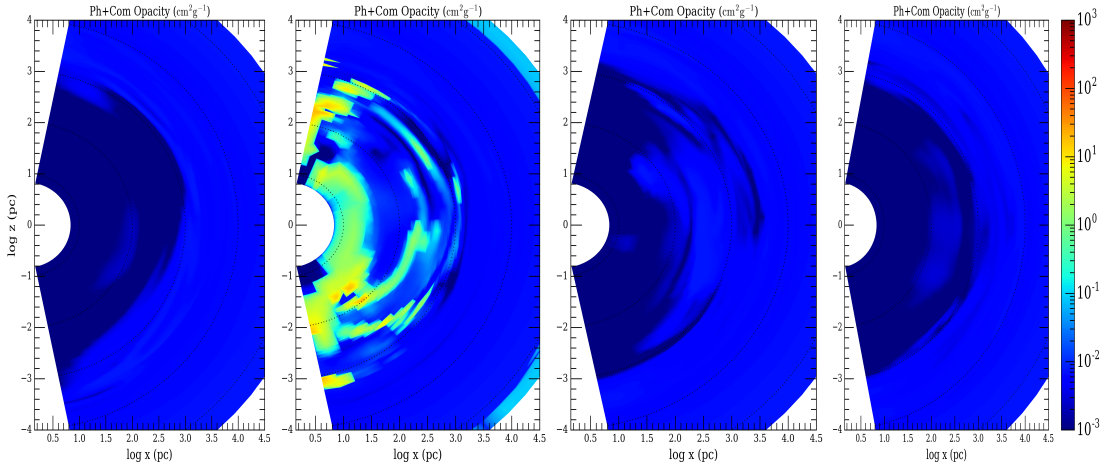

Figure 4.8: Maps of photoionization opacity in cm^2g^{-1} computed with $L_{BH,X}$, at the representative times of Fig. 4.1

bands from bolometric accretion luminosity:

$$\kappa_{opt} = \frac{300}{1 + T/10^4} \ , \qquad \kappa_{uv} = 4\kappa_{opt} \ , \qquad \kappa_{ir} = \frac{\kappa_{opt}}{150} \tag{4.1}$$

$$L_X = 0.7 L_{BH} \ , \qquad L_{uv} = 0.2 L_{BH} \ , \qquad L_{opt} = 0.1 L_{BH} \tag{4.2}$$

In Fig. 4.8 we show the photoionization opacity with the central boundary condition $L_X = 0.7 L_{BH}$ using this; we have computed the radiative transfer for the same time of section 4.2.1, using 4.1 and 4.2 (Fig. 4.9).

We can see that the interesting situation is when the outburst is ongoing: we have that in the X ray band (top row of fig. 4.9) the global regime is optically thin, except for the absorbing feature that we can see in the second panel from the left where light is absorbed up to $\sim 90\%$, but just in certain line of sight; in the UV (central row) and Optical (bottom row) we can see a very different features in the time when the MBH is active: we have an absorption in every direction of propagation of light. Absorbed light is at least $\sim 40\%$ in the UV and $\sim 20\%$ in the Optical band, and in certain line of sight light drops to zero.

Another interesting thing can be extracted from these maps: processes that absorb light in the X band starts to act at radius $R \gtrsim 50\ pc$, while dust starts to absorb light around $\sim few\ pc$; under certain conditions, UV and Optical light is absorbed in the first $\sim 50\ pc$.

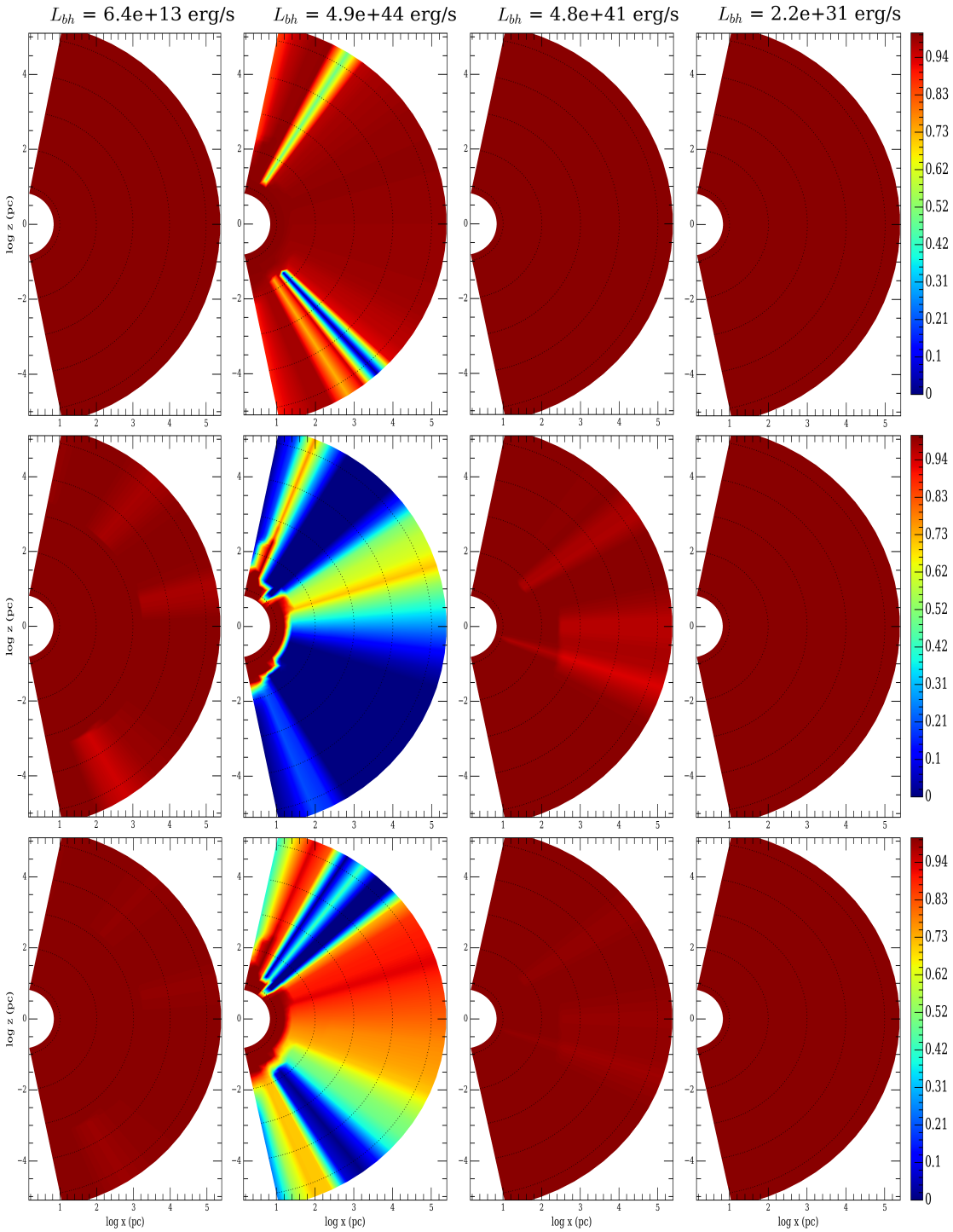

Figure 4.9: Luminosity computed with the D Model and the presence of dust. Top row: L_X^{eff}/L_{BH}^X ; Central row: L_{UV}^{eff}/L_{BH}^{UV}; Bottom row: $L_{Opt}^{eff}/L_{BH}^{Opt}$. The times are the same as in 4.1.

In Fig. 4.10 we can look at global properties of the unabsorbed light from the central MBH which is given by:

$$L^{eff}_{BH,tot}(r) = L^{eff}_{BH,X}(r) + L^{eff}_{BH,UV}(r) + L^{eff}_{BH,Opt}(r) \ , \tag{4.3}$$

and also its impact on the ISM through radiative pressure(Fig. 4.11); bolometric light spreads from $\sim 0.01\%$ to $\sim 80\%$.

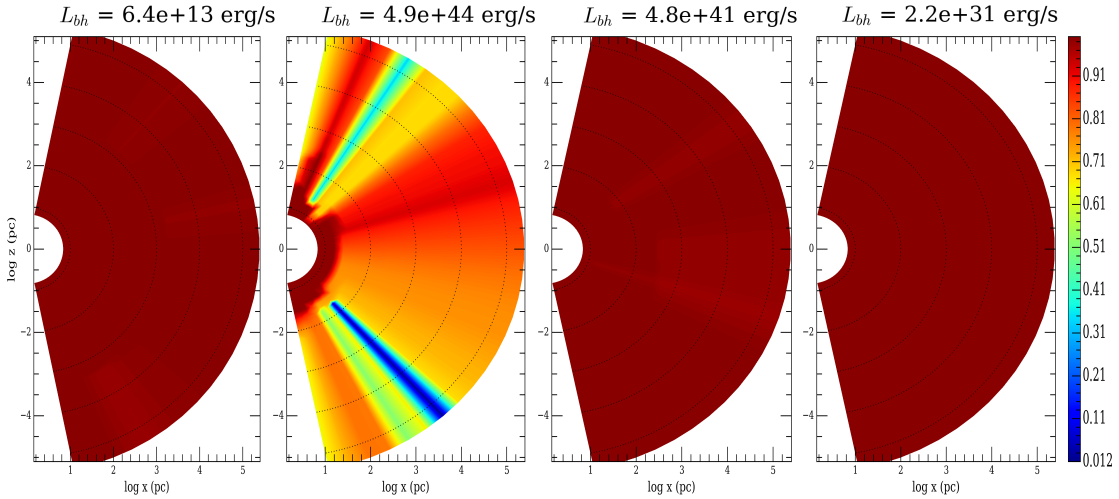

Figure 4.10: $L^{eff}_{BH}/L^{bolo}_{BH}$ with the D model in presence of dust. The times are the same as in 4.1.

From a comparison of Fig. 4.10 and Fig. 4.11 we see that radiation pressure has a drop just where light is more absorbed.

For D Model we do not have major of differences between the ISM modeling in which we have just photoionization and Compton processes and the other in which we have added dust physics. Anyway, we should add the reprocess of light to the IR band due to dust thermalization, and in some cases we can have that $\tau_{ir} \gtrsim 1$ and can be an important radiative pressure term, because sometimes the absorbed light can be of an order of $\sim 40 - 50\%$ of the total light. We plan to run simulations with the full equations of radiative transfer activated, including the radiation reprocessing in order to complete this study.

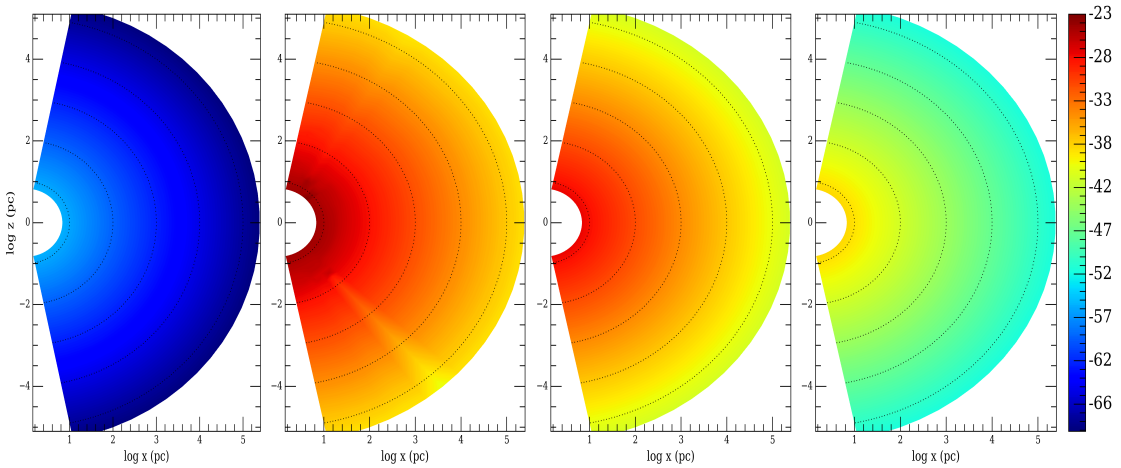

Figure 4.11: $log_{10}\nabla P_{RAD}$ of $L^{eff}_{BH,bolo}$ with the D model in presence of dust. The times are the same as in 4.1.

4.3 AD Model

4.3.1 Photoionization Physics

In the following we have done the same study of section 4.2, but we have applied the AD Model. The computational cost is greater than the one used for the D Model, because the equations (2.137 and 2.138) must be solved iteratively, as we have explained in section 2.6.

In this section we have modelled the ISM with just the photoionization physics; we can see from Fig. 4.12 that we have a greater absorption than the case of D Model application. This is obvious, because in equation 2.137 there is an additive term which subtracts light from the direction of propagation of the light: this is the effect of electron scattering, which removes light from the line of sight and redistributes it isotropically. So, in a first approximation, we can say that the AD Model absorbs more than the D Model.

We have that in the cones in which light is totally absorbed, the pressure gradient drops to ∼zero. It is very difficult to say what implications these drops in radiative pressure can have on gas dynamics: in first approximation, we can imagine that the drop in radiative pressure can decrease the support on the gas, which can fall more rapidly, and it can accrete on the MBH; on the other hand, we have that the missing radiation can allow the gas to cool more rapidly, and then star formation can occur (which means that there is less available gas for MBH accretion).

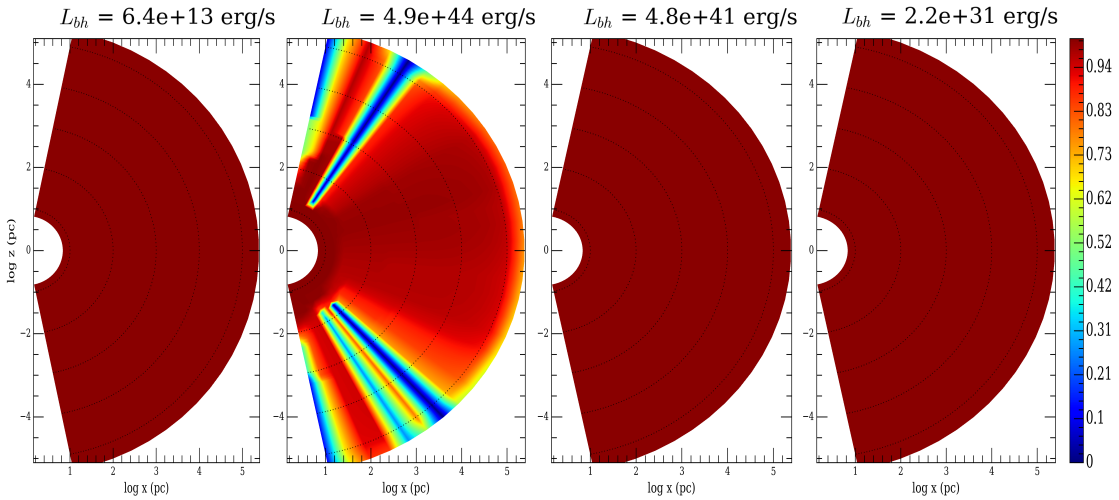

Figure 4.12: $L_{BH}^{eff}/L_{BH}^{bolo}$ with the AD model in absence of dust. The times are the same as in 4.1.

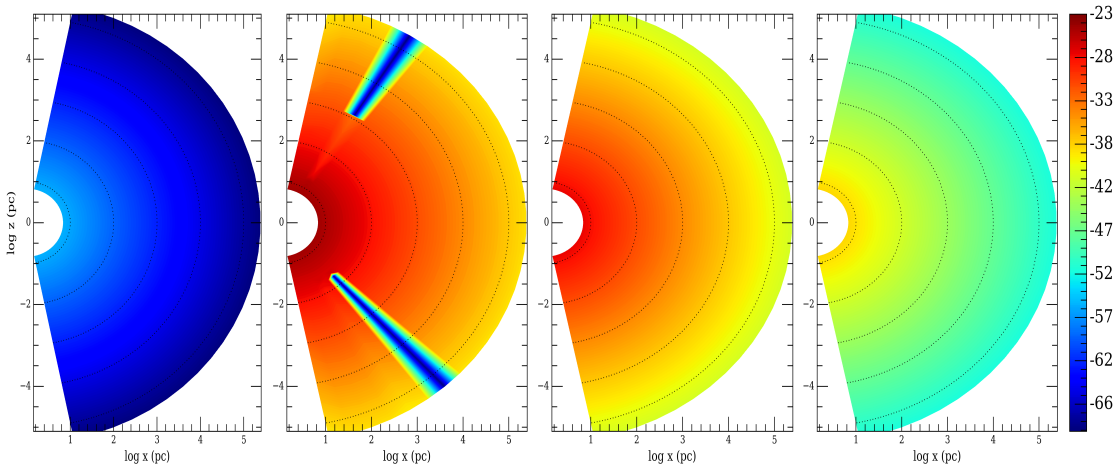

Figure 4.13: $log_{10}\nabla P_{RAD}$ $(cm\ g\ s^{-2})$ of $L_{BH,bolo}^{eff}$ with the AD model in absence of dust. The times are the same as in 4.1.

We can see also another interesting thing: while in the D Model we have just "shadows" behind the high opacity "clump", we have that in this model, beyond the shadows, we have also an absorbing features which nearly smooth, which increases radius by radius: this is the effect that we have mentioned just a little before, due to electron scattering.

4.3.2 Photoionization and Dust Physics

As we have done before, here we analysed the effects of adding dust physics, with the same opacity and division in bands for the bolometric luminosity that we have used in section 4.2.2.

With the addition of dust, we have similar results of absorption computed with the D Model, but we also have more absorbed light. As we can see in Fig. 4.14, central and bottom rows, the UV and Optical light is totally absorbed in the first $\sim 20 - 50$ pc by dust; it reproduced the heavily absorbed quasars, which do not have Optical and UV radiation because it is totally absorbed by the dusty torus, and it implies that a large amount of radiation is emitted in the IR band.

We can see the same smooth absorbing features of section 4.3.1, because of the electron scattering. Also in less optically thick situations (first and third panel from the left) we can see that dust absorbs UV and Optical light respectively for the $\sim 25\%$ and the $\sim 15\%$.

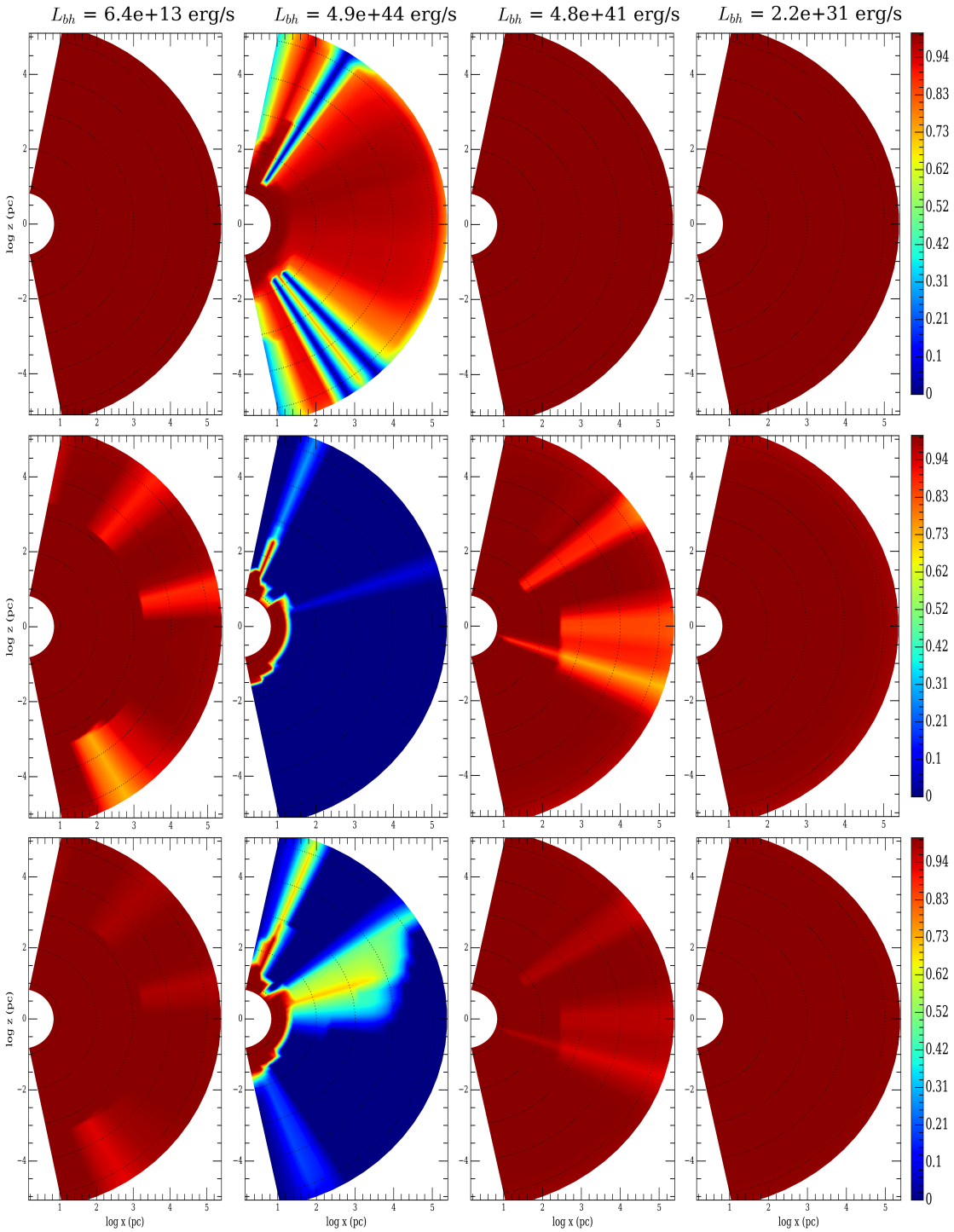

Figure 4.14: Luminosity computed with the AD Model and the presence of dust. Top row: L_X^{eff}/L_{BH}^X ; Central row: L_{UV}^{eff}/L_{BH}^{UV}; Bottom row: $L_{Opt}^{eff}/L_{BH}^{Opt}$. The times are the same as in 4.1.

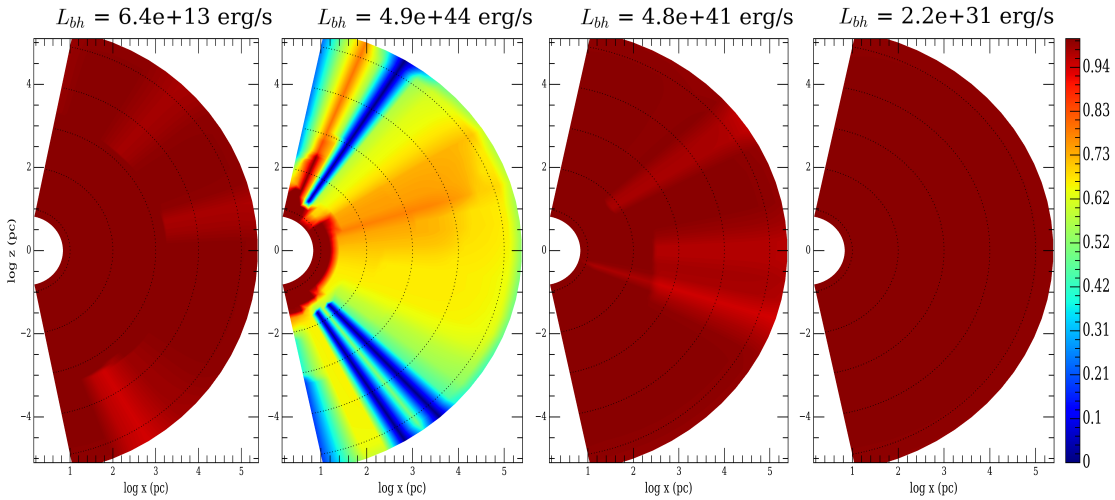

Figure 4.15: $L^{eff}_{BH}/L^{bolo}_{BH}$ with the AD model with of dust. The times are the same as in 4.1.

Finally we show the total accretion luminosity (Fig. 4.15) in order to quantify the amount of radiation that can escape of the galaxy: we can see that only a part of the X-ray radiation reaches the outer radius of the galaxy, and that UV and Optical radiation is totally absorbed. Along certain line of sight radiation cannot escape because of the dramatic absorption, but theoretically, we can have a very high IR flux of reprocessed (IR) light from dust.

From the radiative pressure gradient maps (Fig. 4.16) we can see that where light drops

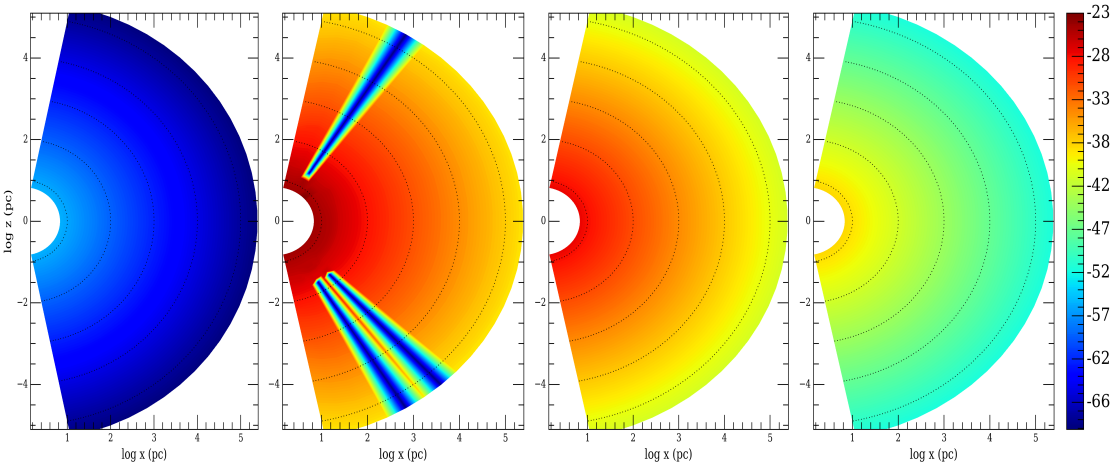

Figure 4.16: $log_{10}\nabla P_{RAD}$ $(cm\ g\ s^{-2})$ of $L^{eff}_{BH,bolo}$ with the AD model with dust. The times are the same as in 4.1.

to zero, also the radial forces drop. So, in the more accurate AD Model we have that the

ISM is absorbing more than the D Model, which leads to a drop in forces on gas.

To understand the implications of these results, we plan to run hydro simulations in order to look at global properties (such as black hole mass accretion, duty cycle of AGN) and to deepen our understanding of the role of dust in AGN feedback.

4.4 AD Model vs. N12 Model

Now we take the moments in μ of order 0, 1 and 2 of I as we have done in chapter 2:

$$J \equiv \frac{1}{4\pi}\int_0^{2\pi} d\phi \int_{-1}^{1} I(\mu,\phi)d\mu = A + \frac{D}{4} \tag{4.4}$$

$$F \equiv \int_0^{2\pi} d\phi \int_{-1}^{1} \mu I(\mu,\phi)d\mu = \frac{4\pi B}{3} + \pi D \tag{4.5}$$

$$P \equiv \frac{1}{c}\int_0^{2\pi} d\phi \int_{-1}^{1} \mu^2 I(\mu,\phi)d\mu = \frac{4\pi A}{3c} + \frac{\pi D}{c} \tag{4.6}$$

To find the appropriate equations, the authors of Novak et al. (2012) have taken two moments of equation 2.15 in two different cases. First, when the radiation field is mildly anisotropic ($D = 0$) with the closure relation $P = 4\pi J/3c$, yielding the differential equations for the photon field in the classic *Eddington approximation*:

$$\frac{dL}{dr} = 4\pi r^2 \left(\dot{E} - 4\pi\rho\kappa_\alpha J\right) \tag{4.7}$$

$$\frac{dJ}{dr} = -\frac{3\rho\left(\kappa_\alpha + \kappa_s\right)L}{16\pi^2 r^2} \tag{4.8}$$

Where the main quantities in these equation are the same defined in chapter 2; After that, when the radiation field is highly directed ($A = B = 0,\ D > 0$) with the closure relation $P = 4\pi J/c$, appropriate for a point source. In this case, the equation for dL/dr is the same and the equation for mean intensity becomes:

$$\frac{dJ}{dr} = -\frac{2J}{r} - \frac{\rho\left(\kappa_\alpha + \kappa_s\right)L}{16\pi^2 r^2} \tag{4.9}$$

After that, the authors have combined equations 4.8 and 4.9 for dJ/dr by introducing the variable t that interpolates between the optically thin (radiation field like a point source) and optically thick (radiation field nearly isotropic) cases. This gives:

$$\frac{dL}{dr} = 4\pi r^2 \left(\dot{E} - 4\pi\rho\kappa_\alpha J\right) \tag{4.10}$$

$$\frac{dJ}{dr} = -\frac{2Jt}{r} - \frac{(3-2t)\rho\left(\kappa_\alpha + \kappa_s\right)L}{16\pi^2 r^2} \tag{4.11}$$

where $t = 0$ when the radiation field is nearly isotropic and $t = 1$ when it is highly directed; so t is defined as follow:

$$1 - t(r) \equiv \frac{1}{1 + e^{5(1-\tau_{in})} + e^{5(1-\tau_{out})}} \ , \tag{4.12}$$

where

$$\tau_{in} = \int_0^r \rho(\kappa_\alpha + \kappa_s) dr \tag{4.13}$$

and

$$\tau_{out} = \int_r^\infty \rho(\kappa_\alpha + \kappa_s) dr \ . \tag{4.14}$$

For detail of this model, see Novak et al. (2012).

Here we have computed the effective accretion luminosity in the X, UV and Optical

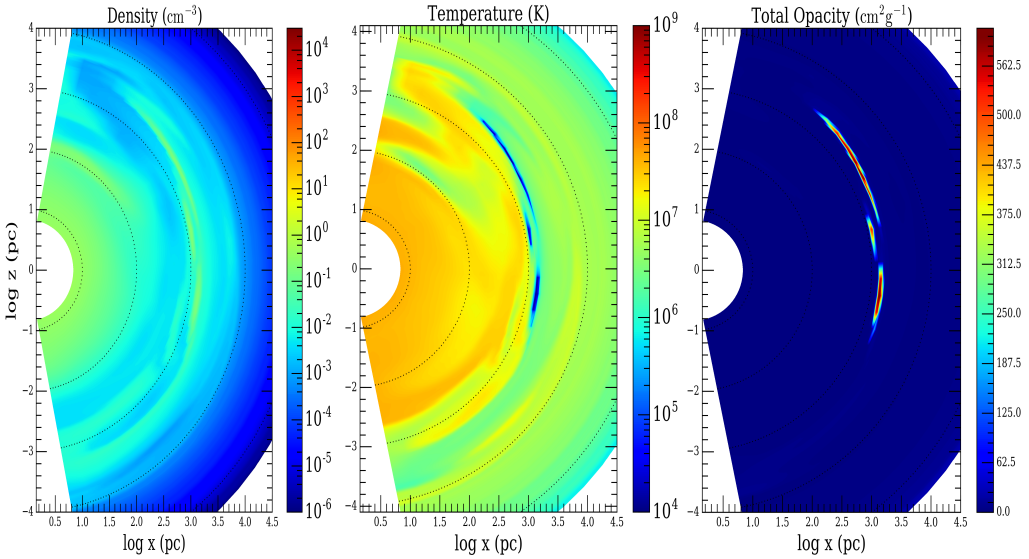

Figure 4.17: From the left to the right panel: density, temperature and dust opacity fields at the representative time of low values of dust opacity ($t \sim 7.12$ Gyr of our simulation)

bands; for each band we have solved the equation of radiative transfer with the AD Model and the N12 Model separately using the photoionization opacity for $L^{eff}_{BH,X}$ and dust opacity for $L^{eff}_{BH,UV}$ and $L^{eff}_{BH,Opt}$. Finally we show the $L^{eff}_{BH,tot}(r)/L_{BH}$, where:

$$L^{eff}_{BH,tot}(r) = L^{eff}_{BH,X}(r) + L^{eff}_{BH,UV}(r) + L^{eff}_{BH,Opt}(r) \ . \tag{4.15}$$

In Fig. 4.18 we show the differences between the two models in a totally optically thin medium. As we can see, the two models show the same radiation field.

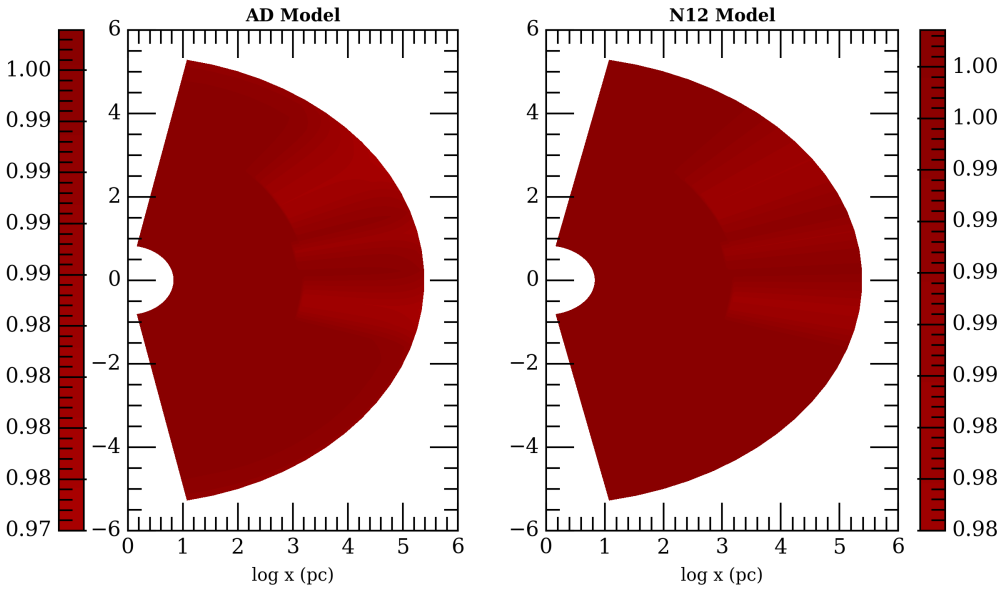

Figure 4.18: Maps of $L^{eff}_{BH,tot}(r)/L_{BH}$ in a totally optically thin ISM.

In Fig. 4.20 we show an intermediate situation: in this one there are a medium a medium that switches from an optically thin to an optically thick one gradually, with an optical depth that reaches a values slightly higher than ~ 1.

In this case the AD Model seems to absorb a little more than the N12 Model in the optically thin region. The features that we can see in this region suggest that probably in the AD Model the electron scattering have a greater effect on radiation. In the last case (Fig. 4.22) we have chosen an extremely optically thick medium, where the optical depth is very high (in Fig. 4.21 we can see that there are some high "opacity clouds" where the ISM is dense and cold); the radiation computed with the AD Model is absorbed $\sim 20\%$ more than that computed with the N12 Model.

Anyway, these are the global trend, involving three different opacities and solving the radiative transfer equations separately.

Now we present a case in which we have computed just one radiative system, so we have solved the A and D equations just for the UV band, in order to better understand how the model works. We present in Fig. 4.24 the maps of $L^{eff}_{BH,UV}(r)$, so the UV part of the bolometric accretion luminosity which be absorbed by dust (so using UV opacity in the 3.29). Here we can see that despite the low τ in some regions, we have continuous absorption of radiation in the AD Model, while in the N12 Model this does not happen. These differences between the models is due to electron scattering, as a confirmation of what said above. Furthermore, if we take $\kappa_{es} \to 0$ the resulting radiation field tends to the radiation field computed with N12 Model, and both tend to the field computed to the D Model; on the other hand, the radiation field computed with the N12 Model has a difference with $\kappa_{es} \sim \kappa_{UV}$, so when κ_{es} becomes $\sim 10^3$ times higher, as we have seen

in section 3.3. We must investigate about this fact, because we have to understand if the AD Model is too sensitive to the scattering parameter or the N12 Model is too little sensitive to the scattering parameter.

We note that however, in extremely optically thick region, both models behave as the D Model.

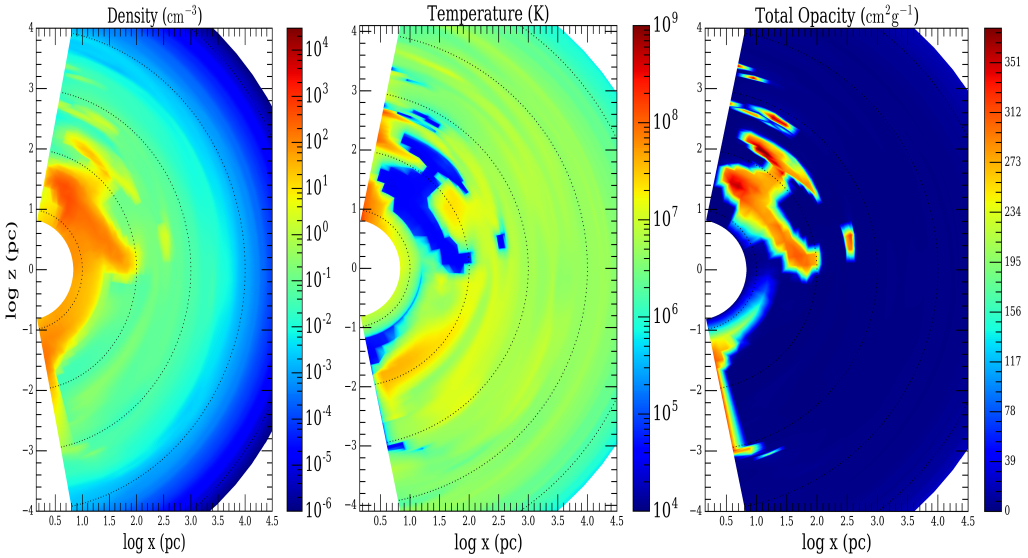

Figure 4.19: From the left to the right panel: density, temperature and dust opacity fields at the representative time of low values of dust opacity ($t \sim 2$ Gyr of our simulation).

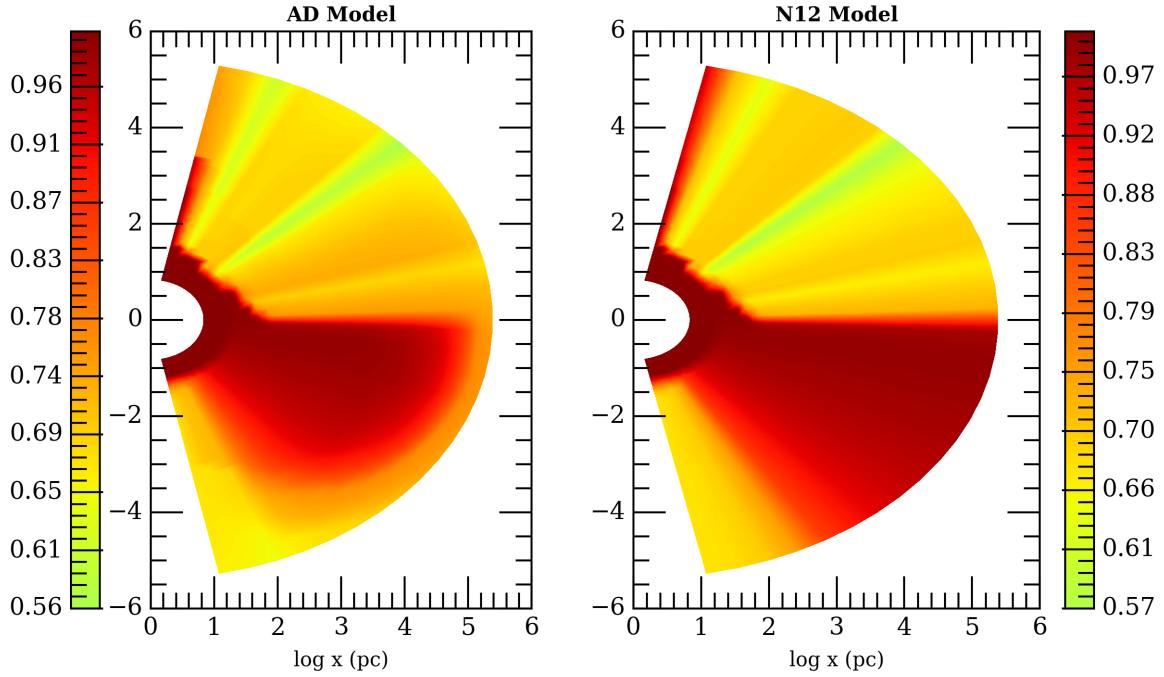

Figure 4.20: Maps of $L^{eff}_{BH,tot}(r)/L_{BH}$ in the time of 4.19.

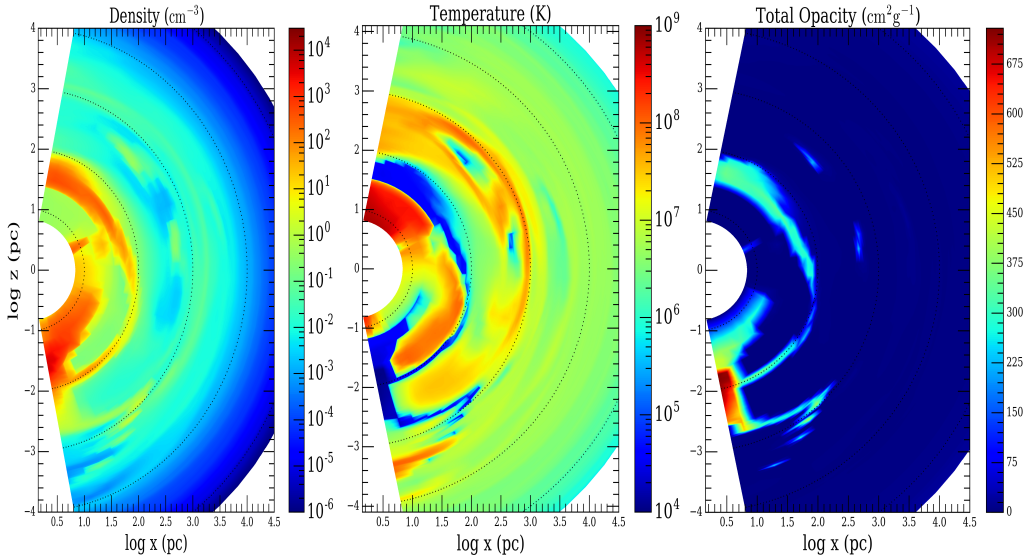

Figure 4.21: From the left to the right panel: density, temperature and dust opacity fields at the representative time of high values of dust opacity ($t \sim 2$ Gyr of our simulation).

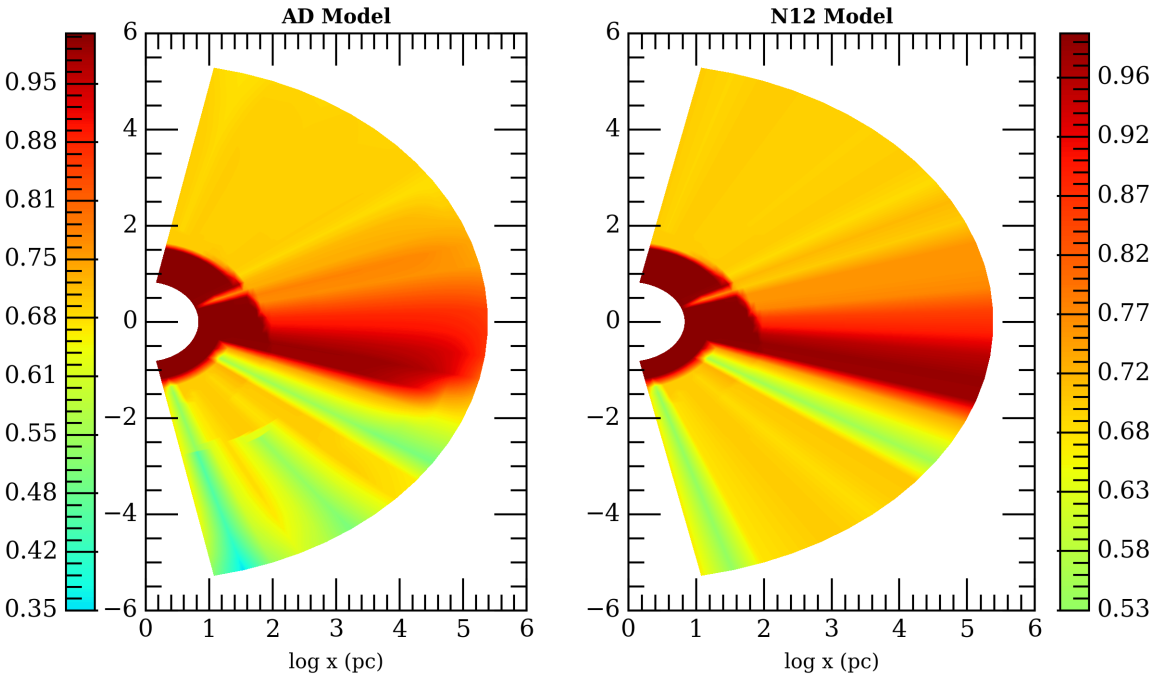

Figure 4.22: Maps of $L^{eff}_{BH,tot}(r)/L_{BH}$ in the time of 4.21.

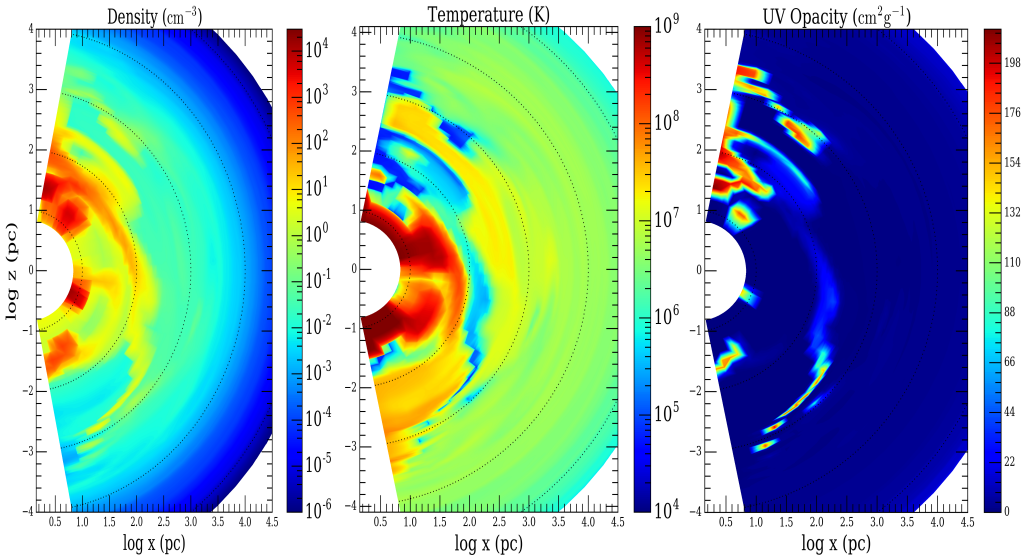

Figure 4.23: From the left to the right panel: density, temperature and dust opacity fields at the representative time of high values of dust UV opacity ($t \sim 2$ Gyr of our simulation).

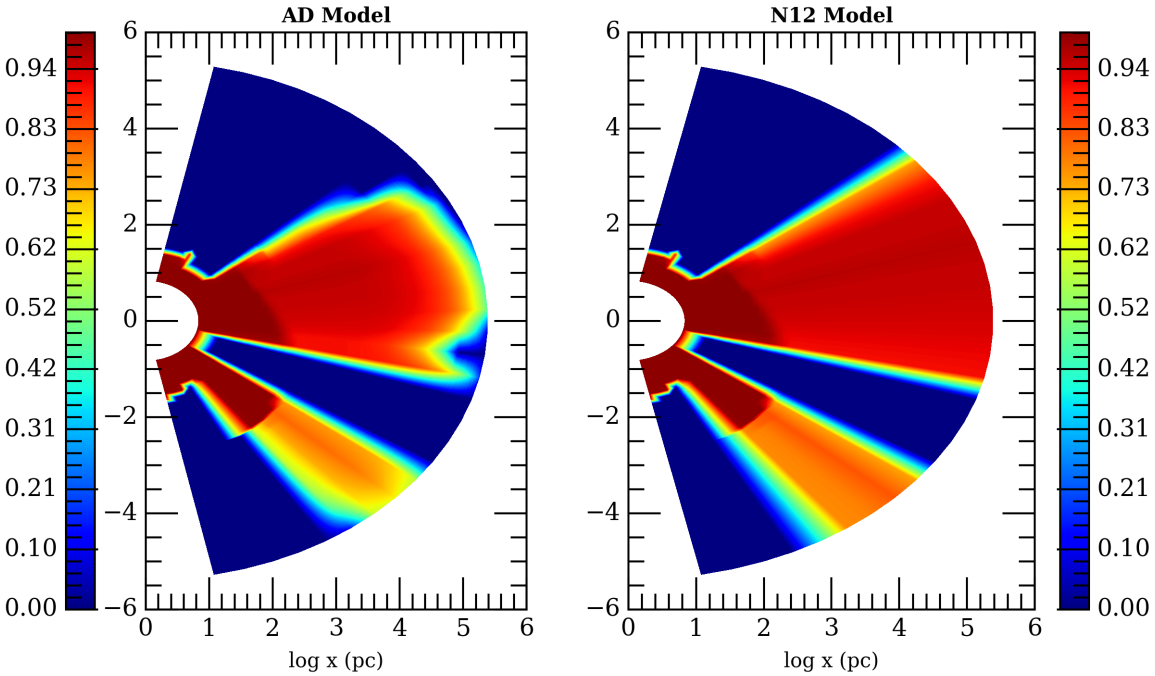

Figure 4.24: Maps of $L^{eff}_{BH,UV}(r)/L_{BH}$ in the time of 4.23.

Chapter 5

Discussions and Conclusions

In this work we have studied a new model of radiative transfer, optimized for the treatment of QSO activity that can occur in Elliptical galaxies. In these galaxies the ISM is hot and it is often optically thin, however, it can experience a recurrent increase of the mass content of cold gas and dust, due to thermal instabilities of the hot halo which drives to formation of incipient cooling flows. The cold gas is not important for the mass budget of the ISM, but it can be very important for the radiative properties of AGN (such as LIRGs and ULIRGs, where a major part of the IR radiation is due to star formation and/or to AGN light reprocessed by dust) and to determine the strength of radiative pressure on the ISM, which shapes the environment and can drive winds or outflows.

In order to obtain a physically consistent modeling of the radiative transfer equations, we first derived the equation for the intensity field in spherical symmetry and we constructed the general moment equations. We then fixed an "Ansatz" for the intensity field, by using phenomenological arguments as follows:

We worked with three terms, that we call A, B and D. The first and the second terms together constitute the so-called *Eddington approximation*, which correspond to an intensity I written in the form : $I(r) = A(r) + \mu B(r)$, where μ is the cosine of the angle between the radial direction and the propagation direction. A and B describe the isotropic and the mildly anisotropic radiation fields, as we have shown in chapter 2. Practically, the first term describes an intensity field which is isotropic, and the second describes an intensity field which deviates slightly from the isotropy. The ISM of elliptical galaxies is often optically thin (Chapter 3), and when the AGN inside these galaxies is in the "on phase", the radiation field is highly directed. To model this radiation field we added an additional term which is a function of the radial coordinate (as A and B): the D term. Finally we have built the form of the intensity field: $I(r) = A(r) + \mu B(r) + D(r)\delta(\mu - 1)$, with one term isotropic, one mildly anisotropic and one highly directed.

We have taken into account two cases for this work: the first is the *pure D Model*, $I(r) = D(r)\delta(\mu - 1)$, which has often been used in other works, and the other is the *AD Model*, $I(r) = A(r) + D(r)\delta(\mu - 1)$. In our working hypotheses the "$A + D$" Ansatz

works well when we want to solve the radiative transfer in galaxies with AGN, because the AD Model can switches from an optically thick regime (where the intensity field is dominated by the A term) to the optically thin one (in which the D term dominates the intensity field).

We have studied the behaviour of the radiative transfer equation in different regimes, elucidating the role of the A, B and D fields and their link with geometrical and physical aspects that should be important in galaxies with an AGN; most of this work is original. We have also determined the analytical solution for some of these models. This is quite a remarkable result, as the solution of radiative transfer in different geometries from plane parallel is notorially difficult, and almost no solutions can be found in the literature.

A second, major step of this work was to test our solutions with adopted density and temperature maps obtained from 2D hydrodynamical simulations; to these maps we associated in post processing the opacity effect of the ISM, using some prescriptions for photoionization and dust physics (Novak et al. 2012, Hensley et al. 2014).

In this way we compared the predictions of our more justified modeling with the usual approach just based on flux absorption (the *pure D Model*), in some interesting cases that occur in galaxies with an AGN: just before, during and after an AGN outburst, in which we have all the ISM physics and phases; this because the AGN outburst is activated by accretion of (cooled) flows, that are generated by thermal instabilities of the hot halo.. This phenomenon leads to an accumulation of a multiphase gas that spreads a lot in temperature and density, and that interacts in very different ways with the radiation; moreover, it occurs when the AGN reaches $L_{BH} \sim L_{Edd}$, so is fundamental to understand the fate of this gas because of radiative feedback from the central MBH.

We found that in the limits of optically thin and thick regimes, the pure D and AD Models both give the same results, as it is expected. For intermediate regimes we have that the AD Model absorbs more than the D Model: this because in our model the electron scattering continues to subtract flux, and distributes it isotropically, while in the pure D Model only the true absorption of the ISM works. In term of radiation pressure gradient, we have seen that the formula to compute it is the same in both D and AD Model, so the differences in the two models reside just in the difference in luminosity that is not absorbed. Probably the interesting cases in ∇P_{RAD} is when light is totally absorbed.

Finally we have also compared the N12 "phenomenological" Model from Novak et al. (2012) with the AD Model. This is important because our solution is exact (in the framework of the adopted Ansatz) but it will be certaintly time-expensive if implemented in full in a hydrodynamical code, so that our solution can be used as a benchmark for faster but approximate solutions. Doing this comparison between our model and N12 Model, we found that some interesting properties of the two models depend on the electron scattering parameter: if we take the $\kappa_{es} \to 0$, the radiation field computed with the AD Model tends to the results found with the N12 Model; on the other hand, the radiation field computed with the N12 Model starts to have changes only for $\kappa_{es} \sim \kappa_{dust}$,

thus, for an electron scattering parameter 1000 times higher. We plan to investigate this fact because we have to understand if the AD Model is too sensitive to the scattering parameter or the N12 Model is too little sensitive to it. However, the general behaviour of these models are similar, especially in the optically thin and thick regimes.

To sum up, by analytical and post processing study, it seems that AD Model can be a good model to fit the AGN feedback radiative problem; however, because of the high computational cost to solve the AD equations, we can use the D model. In addition we have understood that formation of dust, even if for short periods, ca be important to transfer energy and momentum on gas, and to reproduce the IR emission of AGNs.

5.1 Future Prospects

The discussion conducted so far is affected by some apparent simplifications: for example, the X, UV and Optical photons absorbed by dust, are not reprocessed in the IR band. In order to extend this work, we intend to investigate the following aspects.

1. We have to find a way to "recycle" X, UV and Optical radiation which is absorbed and re-emitted in the IR band by dust grains. Even if the infrared opacity has lower values than the Optical or UV opacity, the large amount of recycled photons and as a consequence the IR gradient pressure can have an important role on gas dynamics. With this new implementation we can also compare the total IR emission and compare it with old and future observations (JWST). These will be important for the understanding of LIRGs and ULIRGs.

2. Study the post processing with AGN and discrete input energy source (star formation).

3. Test the ABD Model for radiative transfer, and compare it with the previously model, both analytically and numerically.

4. Find an algorithm that fits the AD Model for numerical simulation.

5. Do hydro simulations and then compare the results (MBH mass, hot gas content, X-Ray luminosity) with other numerical works and observations.

Appendix A

Geometry of Radiative Transfer equation

In any physical problem, the coordinate system plays a fundamental role to resolve it. The coordinate system should be chosen to fit the problem, to exploit any constraint or symmetry present in it. Naturally, for the "conservation law for the difficulty of the problem", there is a price that we must pay for the use of a non-Cartesian coordinate system, such as Curvilinear coordinate system: for this type of coordinate, can be anti-intuitive to understand the position and the direction of a vector that represents the position of a point P in space in relation to an arbitrary reference origin O, idem for the differential operators (such as gradient, divergence and curl).

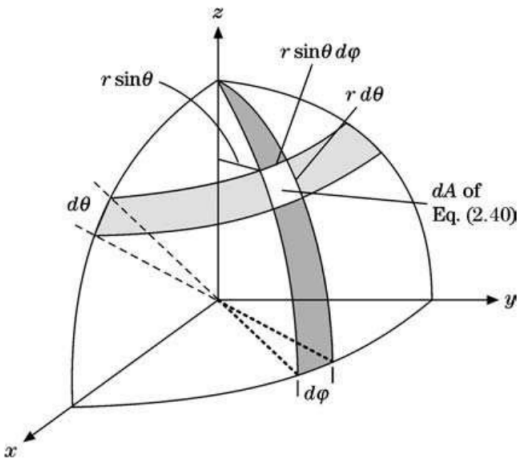

We can imagine that we have I at the radius $\boldsymbol{r}$ and move it in the $\boldsymbol{n}$ direction with a term value $\lambda \in \mathbb{R}$, and we would like to derivative it:

$$I(\boldsymbol{r}, \boldsymbol{n}) \mapsto I(\boldsymbol{r} + \lambda \boldsymbol{n}, \boldsymbol{n}) \tag{A.1}$$

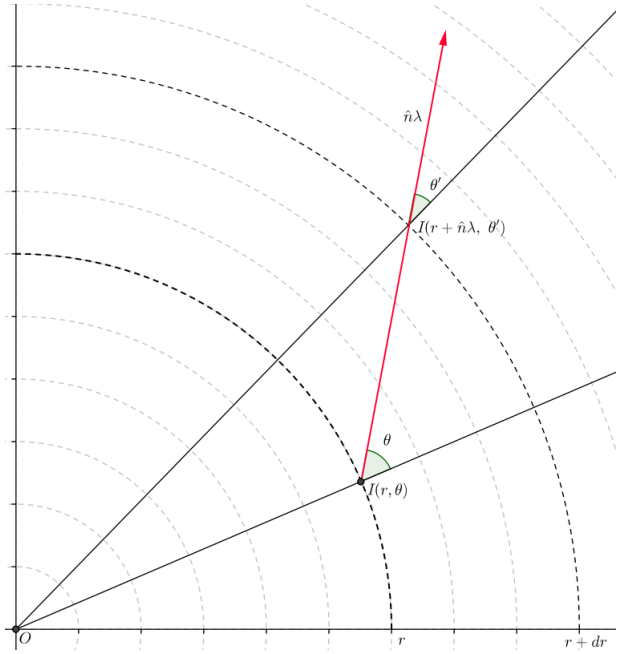

Figure A.1: Geometry for the calculation of the directional derivative. As we can see, $\theta \neq \theta'$.

This is a directional derivative, so the general formula is:

$$\left[\frac{d}{d\lambda} I(\boldsymbol{r}+\lambda\boldsymbol{n},\boldsymbol{n})\right]_{\lambda=0} =< \nabla I, \boldsymbol{n} > \ . \tag{A.2}$$

In this case we have to derivative in $\boldsymbol{r}$ and θ, which is the angle between $\boldsymbol{e_r}$ and $\boldsymbol{n}$:

$$< \nabla_s I, \boldsymbol{n} >=< \nabla_r I, \boldsymbol{n} > + < \nabla_\theta I, \boldsymbol{n} > \ . \tag{A.3}$$

Where the ∇_s means the gradient in spherical coordinates. We now take the first term:

$$< \nabla_r I, \boldsymbol{n} >=< \frac{\partial I}{\partial r}\boldsymbol{e_r}, \boldsymbol{n} >=< \boldsymbol{e_r}, \boldsymbol{n} > \frac{\partial I}{\partial r} \ , \tag{A.4}$$

but $< \boldsymbol{e_r}, \boldsymbol{n} >= \cos(\theta)$, then

$$< \nabla_r I, \boldsymbol{n} >= cos(\theta)\frac{\partial I}{\partial r} \ . \tag{A.5}$$

So, the first term of the derivative is $cos(\theta)\frac{\partial I}{\partial r}$. For the second term we have to be careful,

because of θ changes while we move along $\lambda \boldsymbol{n}$ (Fig. A.1):

$$< \nabla_\theta I, \boldsymbol{n} >= \frac{1}{r} < \frac{\partial I}{\partial \theta} \boldsymbol{e_\theta}, \boldsymbol{n} >= \frac{1}{r} \frac{\partial I}{\partial \theta} < \boldsymbol{e_\theta}, \boldsymbol{n} > \ . \tag{A.6}$$

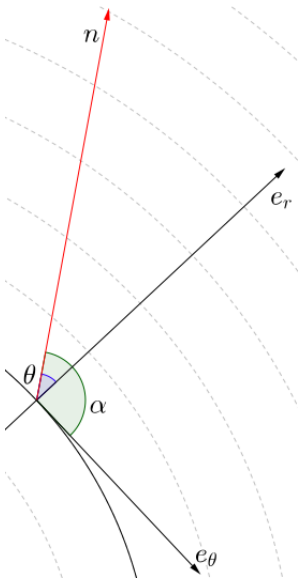

We have that :

$$< \boldsymbol{e_\theta}, \boldsymbol{n} >= cos(\alpha) \tag{A.7}$$

and we have that $\alpha = (\theta + \frac{\pi}{2})$, because for definition the angle between $\boldsymbol{e_r}$ and $\boldsymbol{e_\theta}$ is $\frac{\pi}{2}$, so we can write:

$$cos(\alpha) = cos(\theta + \frac{\pi}{2}) = -sin(\theta) \ . \tag{A.8}$$

Now we rewrite the A.6 using the A.8:

$$< \nabla_\theta I, \boldsymbol{n} >= -\frac{sin(\theta)}{r} \frac{\partial I}{\partial \theta} \ , \tag{A.9}$$

using the chain rule we can write:

$$\frac{\partial I}{\partial \theta} = \frac{\partial I}{\partial cos(\theta)} \frac{\partial cos(\theta)}{\partial \theta} = -sin(\theta) \frac{\partial I}{\partial cos(\theta)} \ , \tag{A.10}$$

because

$$\frac{\partial cos(\theta)}{\partial \theta} = -sin(\theta) \ . \tag{A.11}$$

We insert the A.10 in the A.9, we obtain:

$$< \nabla_\theta I, \boldsymbol{n} >= \frac{sin^2(\theta)}{r} \frac{\partial I}{\partial cos(\theta)} \ , \tag{A.12}$$

and knowing that $cos^2(\theta) + sin^2(\theta) = 1$, we can finally write:

$$< \nabla_\theta I, \boldsymbol{n} >= \frac{1 - cos^2(\theta)}{r} \frac{\partial I}{\partial cos(\theta)} \ . \tag{A.13}$$

To conclude, we gather the A.5 and the A.13:

$$< \nabla_s I, \boldsymbol{n} >= cos(\theta) \frac{\partial I}{\partial r} + \frac{1 - cos^2(\theta)}{r} \frac{\partial I}{\partial cos(\theta)} \ . \tag{A.14}$$

Finally we can write:

$$< \nabla_s I, \boldsymbol{n} >= \mu \frac{\partial I}{\partial r} + \frac{1 - \mu^2}{r} \frac{\partial I}{\partial \mu} \ , \tag{A.15}$$

where we have called $cos(\theta) = \mu$.
To sum up, this is the way to write the derivative of $I(r, \mu)$ in curvilinear coordinate in spherical symmetry:

$$\left[\frac{d}{d\lambda} I(\boldsymbol{r} + \lambda \boldsymbol{n}, \boldsymbol{n}) \right]_{\lambda=0} = \mu \frac{\partial I}{\partial r} + \frac{1 - \mu^2}{r} \frac{\partial I}{\partial \mu} \tag{A.16}$$

because as we move along a direction, the coordinate under our feet changes. This is the same result that we can find in *Radiative Transfer*, S. Chandrasekhar (1950).

Bibliography

Alexander, D. M. and R. C. Hickox (2012). "What drives the growth of black holes?" In: 56, pp. 93–121. DOI: 10.1016/j.newar.2011.11.003. arXiv: 1112.1949.

Bahcall, J. N. et al. (1997). "Hubble Space Telescope Images of a Sample of 20 Nearby Luminous Quasars". In: 479, pp. 642–658. DOI: 10.1086/303926. eprint: astro-ph/9611163.

Chandrasekhar, S. (1950). *Radiative transfer.*

Ciotti, L. (2009). "Co-evolution of elliptical galaxies and their central black holes. Clues from their scaling laws." In: *Nuovo Cimento Rivista Serie* 32, pp. 1–69. DOI: 10.1393/ncr/i2008-10040-2. arXiv: 0808.1349.

Ciotti, L., A. D'Ercole, et al. (1991). "Winds, outflows, and inflows in X-ray elliptical galaxies." In: 376, pp. 380–403. DOI: 10.1086/170289.

Ciotti, L. and J. P. Ostriker (1997). "Cooling Flows and Quasars: Different Aspects of the Same Phenomenon? I. Concepts". In: 487, pp. L105–L108. DOI: 10.1086/310902. eprint: astro-ph/9706281.

— (2001). "Cooling Flows and Quasars. II. Detailed Models of Feedback-modulated Accretion Flows". In: 551, pp. 131–152. DOI: 10.1086/320053. eprint: astro-ph/9912064.

— (2007). "Radiative Feedback from Massive Black Holes in Elliptical Galaxies: AGN Flaring and Central Starburst Fueled by Recycled Gas". In: 665, pp. 1038–1056. DOI: 10.1086/519833. eprint: astro-ph/0703057.

Ciotti, L., J. P. Ostriker, G. Novak, et al. (2015). "AGN feedback and star formation in ETGs: negative and positive feedback". In: *IAU General Assembly* 22, 2256683, p. 2256683. arXiv: 1511.00510.

Ciotti, L., J. P. Ostriker, and D. Proga (2010). "Feedback from Central Black Holes in Elliptical Galaxies. III. Models with Both Radiative and Mechanical Feedback". In: 717, pp. 708–723. DOI: 10.1088/0004-637X/717/2/708. arXiv: 1003.0578.

Ciotti, L., S. Pellegrini, et al. (2017). "The Effect of the AGN Feedback on the Interstellar Medium of Early-Type Galaxies:2D Hydrodynamical Simulations of the Low-Rotation Case." In: 835, 15, p. 15. DOI: 10.3847/1538-4357/835/1/15. arXiv: 1608.03403.

Dunlop, J. S. et al. (2003). "Quasars, their host galaxies and their central black holes". In: 340, pp. 1095–1135. DOI: 10.1046/j.1365-8711.2003.06333.x. eprint: astro-ph/0108397.

Fabbiano, G. (1989). "X rays from normal galaxies". In: 27, pp. 87–138. DOI: 10.1146/annurev.aa.27.090189.000511.

Fabian, A. C. (1994). "Cooling Flows in Clusters of Galaxies". In: 32, pp. 277–318. DOI: 10.1146/annurev.aa.32.090194.001425.

— (2012). "Observational Evidence of Active Galactic Nuclei Feedback". In: 50, pp. 455–489. DOI: 10.1146/annurev-astro-081811-125521. arXiv: 1204.4114.

Fabian, A. C. et al. (2006). "A very deep Chandra observation of the Perseus cluster: shocks, ripples and conduction". In: 366, pp. 417–428. DOI: 10.1111/j.1365-2966.2005.09896.x. eprint: astro-ph/0510476.

Ferrarese, L. and D. Merritt (2000). "A Fundamental Relation between Supermassive Black Holes and Their Host Galaxies". In: 539, pp. L9–L12. DOI: 10.1086/312838. eprint: astro-ph/0006053.

Gebhardt, K., R. Bender, et al. (2000). "A Relationship between Nuclear Black Hole Mass and Galaxy Velocity Dispersion". In: 539, pp. L13–L16. DOI: 10.1086/312840. eprint: astro-ph/0006289.

Gebhardt, K., D. Richstone, et al. (2000). "Axisymmetric, Three-Integral Models of Galaxies: A Massive Black Hole in NGC 3379". In: 119, pp. 1157–1171. DOI: 10.1086/301240. eprint: astro-ph/9912026.

Greggio, L. (2010). "The rates of SNIa: a theoretical viewpoint". In: *Progenitors and Environments of Stellar Explosions*, p. 65.

Hamann, F. et al. (2008). "Emergence of a quasar outflow". In: 391, pp. L39–L43. DOI: 10.1111/j.1745-3933.2008.00554.x. arXiv: 0808.3998.

Hayes, J. C. et al. (2006). "Simulating Radiating and Magnetized Flows in Multiple Dimensions with ZEUS-MP". In: 165, pp. 188–228. DOI: 10.1086/504594. eprint: astro-ph/0511545.

Hensley, B. S. et al. (2014). "Grain Physics and Infrared Dust Emission in Active Galactic Nucleus Environments". In: 789, 78, p. 78. DOI: 10.1088/0004-637X/789/1/78. arXiv: 1402.6325.

Hummel, E. (1981). "Central radio sources in galaxies". In: *Origin of Cosmic Rays*. Ed. by G. Setti et al. Vol. 94. IAU Symposium, p. 167.

Kennicutt Jr., R. C. et al. (1987). "The effects of interactions on spiral galaxies. II - Disk star-formation rates". In: 93, pp. 1011–1023. DOI: 10.1086/114384.

Kormendy, J. and L. C. Ho (2013). "Coevolution (Or Not) of Supermassive Black Holes and Host Galaxies". In: 51, pp. 511–653. DOI: 10.1146/annurev-astro-082708-101811. arXiv: 1304.7762.

Magorrian, J. et al. (1998). "The Demography of Massive Dark Objects in Galaxy Centers". In: 115, pp. 2285–2305. DOI: 10.1086/300353. eprint: astro-ph/9708072.

Maoz, D. et al. (2011). "Nearby supernova rates from the Lick Observatory Supernova Search - IV. A recovery method for the delay-time distribution". In: 412, pp. 1508–1521. DOI: 10.1111/j.1365-2966.2010.16808.x. arXiv: 1002.3056.

Maraston, C. (2005). "Evolutionary population synthesis: models, analysis of the ingredients and application to high-z galaxies". In: 362, pp. 799–825. DOI: 10.1111/j.1365-2966.2005.09270.x. eprint: astro-ph/0410207.

Mathews, W. G. (1989). "On the global ecology of elliptical galaxies". In: 97, pp. 42–56. DOI: 10.1086/114955.

— (1990). "Interstellar events in elliptical galaxies". In: 354, pp. 468–482. DOI: 10.1086/168708.

Negri, A. et al. (2015). "X-ray haloes and star formation in early-type galaxies". In: 451, pp. 1212–1228. DOI: 10.1093/mnras/stv968. arXiv: 1501.07111.

Neugebauer, G. et al. (1979). "Absolute spectral energy distribution of quasi-stellar objects from 0.3 to 10 microns". In: 230, pp. 79–94. DOI: 10.1086/157063.

Novak, G. et al. (2012). "Radiative transfer and radiative driving of outflows in active galactic nuclei and starbursts". In: 427, pp. 2734–2756. DOI: 10.1111/j.1365-2966.2012.21844.x. arXiv: 1203.6062.

Ostriker, J. P. et al. (2010). "Momentum Driving: Which Physical Processes Dominate Active Galactic Nucleus Feedback?" In: 722, pp. 642–652. DOI: 10.1088/0004-637X/722/1/642. arXiv: 1004.2923.

Parriott, J. R. and J. N. Bregman (2008). "Mass Loss from Evolved Stars in Elliptical Galaxies". In: 681, 1215-1232, pp. 1215–1232. DOI: 10.1086/588033. arXiv: 0805.4331.

Pellegrini, S. (2012). "Hot Gas Flows on Global and Nuclear Galactic Scales". In: *Astrophysics and Space Science Library*. Ed. by D.-W. Kim and S. Pellegrini. Vol. 378. Astrophysics and Space Science Library, p. 21. DOI: 10.1007/978-1-4614-0580-1_2. arXiv: 1112.2140 [astro-ph.CO].

Sanders, D. B. and I. F. Mirabel (1996). "Luminous Infrared Galaxies". In: 34, p. 749. DOI: 10.1146/annurev.astro.34.1.749.

Sazonov, S. Y., J. P. Ostriker, L. Ciotti, et al. (2005). "Radiative feedback from quasars and the growth of massive black holes in stellar spheroids". In: 358, pp. 168–180. DOI: 10.1111/j.1365-2966.2005.08763.x. eprint: astro-ph/0411086.

Sazonov, S. Y., J. P. Ostriker, and R. A. Sunyaev (2004). "Quasars: the characteristic spectrum and the induced radiative heating". In: 347, pp. 144–156. DOI: 10.1111/j.1365-2966.2004.07184.x. eprint: astro-ph/0305233.

Sharon, K. et al. (2010). "The Type Ia Supernova Rate in Redshift 0.5-0.9 Galaxy Clusters". In: 718, pp. 876–893. DOI: 10.1088/0004-637X/718/2/876. arXiv: 1006.3757.

Toomre, A. and J. Toomre (1972). "Galactic Bridges and Tails". In: 178, pp. 623–666. DOI: 10.1086/151823.